BRIEF DEFINITIVE REPORT

Necroptosis restricts influenza A virus as a stand-alone cell death mechanism

Maria Shubina[1]*, Bart Tummers[2]*, David F. Boyd[2]*, Ting Zhang[1]*, Chaoran Yin[1], Avishekh Gautam[1], Xi-zhi J. Guo[2], Diego A. Rodriguez[2], William J. Kaiser[3], Peter Vogel[2], Douglas R. Green[2], Paul G. Thomas[2], and Siddharth Balachandran[1]

Influenza A virus (IAV) activates ZBP1-initiated RIPK3-dependent parallel pathways of necroptosis and apoptosis in infected cells. Although mice deficient in both pathways fail to control IAV and succumb to lethal respiratory infection, RIPK3-mediated apoptosis by itself can limit IAV, without need for necroptosis. However, whether necroptosis, conventionally considered a fail-safe cell death mechanism to apoptosis, can restrict IAV—or indeed any virus—in the absence of apoptosis is not known. Here, we use mice selectively deficient in IAV-activated apoptosis to show that necroptosis drives robust antiviral immune responses and promotes effective virus clearance from infected lungs when apoptosis is absent. We also demonstrate that apoptosis and necroptosis are mutually exclusive fates in IAV-infected cells. Thus, necroptosis is an independent, "stand-alone" cell death mechanism that fully compensates for the absence of apoptosis in antiviral host defense.

Introduction

Influenza A virus (IAV) replication is typically accompanied by death of the infected cell (Herold et al., 2012; Upton et al., 2017). We and others have recently described a signaling pathway that appears to represent the dominant mechanism by which IAV triggers death in lung epithelial cells and other primary cell types. This pathway is initiated when the host sensor protein Z-DNA–binding protein 1 (ZBP1; also called "DAI" [DNA-dependent activator of IFN regulatory factors]) detects IAV Z-RNAs, activates receptor-interacting serine/threonine-protein kinase 3 (RIPK3), and drives parallel pathways of necroptosis and apoptosis in airway epithelial cells and mouse embryonic fibroblasts (MEFs; Fig. 1 A; Kuriakose et al., 2016; Nogusa et al., 2016; Thapa et al., 2016; Zhang et al., 2020).

Complete elimination of this branched cell death pathway in mice, such as via germline deletion of *Zbp1* or *Ripk3*, renders the animal very susceptible to pulmonary viral replication and lethality (Nogusa et al., 2016; Thapa et al., 2016). Fascinatingly, eliminating only necroptosis signaling, by germline ablation of mixed lineage kinase domain–like (*Mlkl*), does not impinge on the apoptosis axis downstream of RIPK3 and does not significantly impact the anti-IAV immune response (Nogusa et al., 2016). That is, RIPK3-activated apoptosis signaling is largely capable of controlling pulmonary IAV infection on its own. It is unknown, however, if necroptosis can similarly limit IAV as a stand-alone mechanism when apoptosis is absent. This is a

critical unanswered question because necroptosis is conventionally considered a "backup" form of fail-safe cell death that is activated when apoptosis pathways are compromised (e.g., by virus-encoded inhibitors of caspase activity; Mocarski et al., 2014; Upton et al., 2010; Vanden Berghe et al., 2016) and because RIPK3, in some cases, regulates the replication of viruses and other pathogens without triggering cell death (Daniels et al., 2017, 2019; Harris et al., 2015; Sai et al., 2019).

Unfortunately, germline ablation of genes encoding the apoptosis effectors in this pathway (i.e., RIPK1, Fas-associated death domain [FADD], and caspase 8 [Casp8]) results in perinatal (*Ripk1*^{−/−}) or embryonic (*Fadd*^{−/−}, *Casp8*^{−/−}) lethality because each of these proteins also has nonapoptotic roles: they restrict RIPK3 activity and prevent necroptosis during early mammalian development (Dillon et al., 2016).

We have produced a knock-in mouse in which endogenous *Casp8* has been replaced with a mutant allele (*Casp8*[DA]) encoding a Casp8 variant selectively incapable of undergoing the autoprocessing requisite for apoptosis but that preserves Casp8 survival function during mammalian development (Dillon et al., 2012; Kang et al., 2008; Oberst et al., 2011; Philip et al., 2016). Mice homozygous for this allele of *Casp8* are viable and fertile but selectively deficient in Casp8-driven apoptosis (Tummers et al., 2020), and thus they provide the first mammalian system in which to test the sole contribution of necroptosis to ZBP1/RIPK3-mediated IAV clearance.
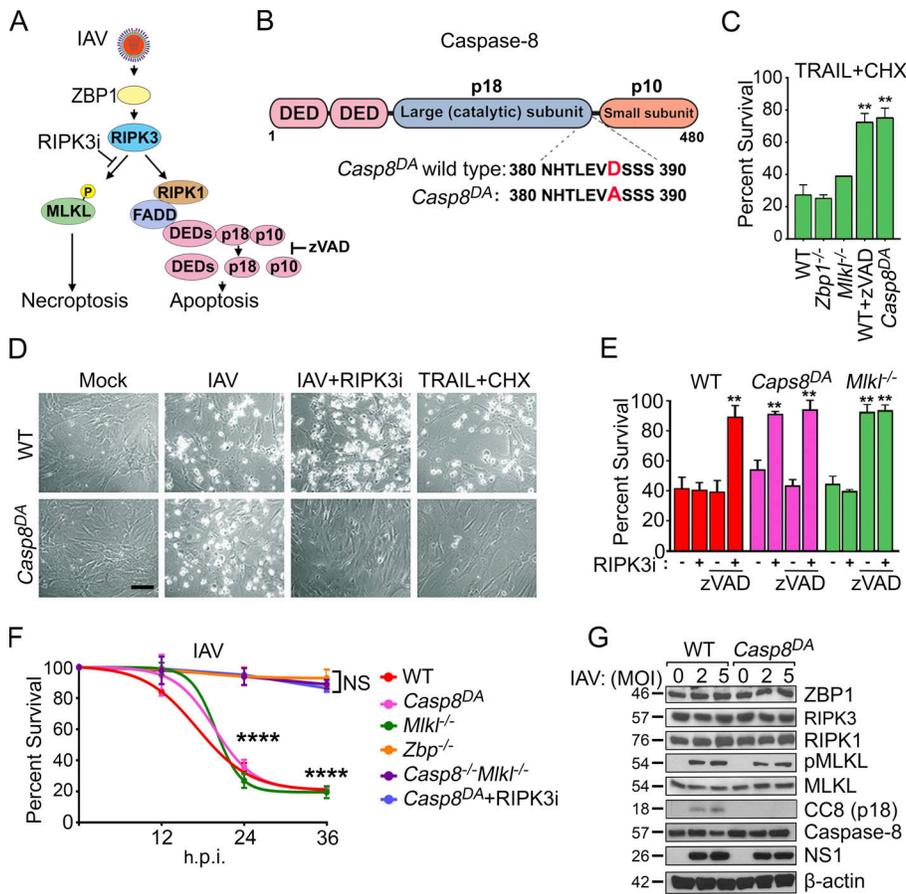
Figure 1. **Casp8^{DA} MEFs are selectively resistant to IAV-induced apoptosis. (A)** ZBP1-RIPK3–dependent cell death pathways activated by IAV. Apoptosis is mediated by RIPK1/FADD-dependent activation of Casp8. **(B)** Casp8 domain organization and knock-in mutation (D387A) in Casp8^{DA} mice. DED, death effector domain. **(C)** MEFs were treated with murine TRAIL (100 ng/ml) in the presence of cycloheximide (CHX; 250 ng/ml), and cell viability was determined at 24 h. n = 3 replicates per condition; data are from one of four experiments with similar results. **(D)** Photomicrographs of WT and Casp8^{DA} MEFs infected with PR8 (multiplicity of infection [MOI], 2) in the presence or absence of RIPK3 inhibitor GSK'843 (5 µM) or treated with TRAIL (100 ng/ml) + CHX (250 ng/ml) for 24 h. Scale bar = 100 µm. **(E)** WT, Casp8^{DA}, or Mlkl$^{-/-}$ MEFs were infected with PR8 (MOI, 2) and exposed to the indicated inhibitors, and cell viability was determined at 24 h postinfection (h.p.i.). n = 3 replicates per condition; data are from one of four experiments with similar results. **(F)** Cell death kinetics after PR8 infection (MOI, 2) of MEFs from the indicated genotypes. n = 3 replicates per condition; data are from one of six experiments with similar results. **(G)** WT and Casp8^{DA} MEFs were infected with PR8 (MOI, 2 or 5) and examined for the indicated proteins at 24 h. Molecular weights in kilodaltons are shown to the left. Results are representative of three independent experiments. Unpaired Student's t test (C and E); two-way ANOVA and Tukey's multiple comparisons test (F). Error bars represent mean ± SD; **, P < 0.005; ****, P < 0.00005.

those from either Zbp1$^{-/-}$ or Mlkl$^{-/-}$ mice, were resistant to TNF-related apoptosis-inducing ligand (TRAIL)–induced, Casp8-dependent apoptosis (Fig. 1 C). The resistance of Casp8^{DA} MEFs to TRAIL-induced apoptosis paralleled the degree of inhibition afforded by the pan-caspase blocker zVAD in WT MEFs (Fig. 1 C). The Casp8 D387A mutation thus effectively abrogates Casp8-driven apoptosis signaling in cells.

Casp8^{DA} MEFs were as susceptible as WT MEFs to IAV-induced death, but a RIPK3 kinase inhibitor, which selectively blocks necroptosis without impeding apoptosis (Mandal et al., 2014), almost completely protected infected Casp8^{DA} MEFs from death (Fig. 1, D–F). In contrast, necroptosis-deficient Mlkl$^{-/-}$ MEFs were not protected from IAV-induced death by a RIPK3 kinase inhibitor, but they were rescued by the pan-caspase inhibitor zVAD (Fig. 1 E). Only combined blockade of apoptosis and necroptosis, via coinhibition of caspase and RIPK3 kinase activities, was capable of preventing cell death in IAV-infected WT MEFs (Fig. 1 E). Similarly, combined genetic deletion of Casp8 and Mlkl, or elimination of Zbp1, protected against IAV-induced cell death in MEFs (Fig. 1 F). Activation of MLKL proceeded normally in IAV-infected Casp8^{DA} MEFs, but cleavage of Casp8 into the p18 fragment was abolished in these cells, despite equivalent levels of upstream cell death effector proteins (i.e., ZBP1 and RIPK3) and comparable levels of virus replication (measured by immunoblotting for the IAV nonstructural

Using Casp8^{DA} mice, we show here that necroptosis on its own limits and clears IAV infection in a manner that is largely indistinguishable from—and in some measures surpasses—IAV clearance in WT control animals. Thus, apoptosis is dispensable for IAV clearance, and necroptosis, often thought of as secondary to apoptosis in host defense, is a potent stand-alone antiviral cell death mechanism in vivo.

Results and discussion

Casp8 activity is required for RIPK3-mediated apoptosis triggered by IAV

Replicating IAV produces Z-RNA species, which are detected by the host sensor ZBP1 (Kuriakose et al., 2016; Thapa et al., 2016; Zhang et al., 2020). ZBP1 then activates RIPK3 to initiate parallel pathways of necroptosis and apoptosis (Nogusa et al., 2016). Apoptosis downstream of RIPK3 is mediated by RIPK1- and FADD-dependent autoproteolytic activation of the Casp8 zymogen into active homodimers consisting of p18 and p10 fragments (Fig. 1 A). We produced Casp8 knock-in mice (Casp8^{DA}) in which the initiation site for autoproteolytic processing of Casp8, essential for its capacity to stimulate apoptosis, was abolished by mutation of a critical aspartic acid to alanine (D387A; Fig. 1 B and Fig. S1, A and B; Kang et al., 2008; Oberst et al., 2011; Philip et al., 2016). Primary early-passage MEFs from Casp8^{DA} mice, but not

protein 1 [NS1]) between WT and *Casp8^DA* MEFs (Fig. 1 G). Collectively, these results demonstrate that cells from the *Casp8^DA* mouse are selectively deficient in activating apoptosis upon IAV infection.

Apoptosis and necroptosis activation are mutually exclusive events in infected cells

In death receptor–mediated apoptosis (e.g., those stimulated by TRAIL and Fas ligand), Casp8 triggers activation of "executioner" caspases, predominantly Casp3, that mediate disassembly and eventual demise of the cell (Ashkenazi and Dixit, 1998). To test if the ZBP1/RIPK3-initiated apoptosis signal also proceeded by similar Casp3-driven mechanisms, we infected WT and *Casp8^DA* MEFs with IAV and monitored Casp3 activity in infected nucleoprotein+ (NP+) cells by staining for cleaved caspase 3 (CC3). Although 30–40% of infected WT MEFs displayed a readily detectable CC3 signal at 18 h, only ~5% of similarly infected *Casp8^DA* MEFs were CC3+ at this time point, indicating that Casp8 was required for activation of Casp3 upon IAV infection (Fig. 2, A and B).

Interestingly, the fraction of NP+ cells also staining positive for CC3 was rarely more than half, although all these cells eventually died. Indeed, dying WT cells displayed either apoptotic or necrotic morphologies; cells displaying features of both necrosis and apoptosis (e.g., both cell swelling and shrunken nuclei) were rarely seen. Because RIPK3 can induce both apoptosis and necroptosis downstream of ZBP1, these observations suggested that, once activated, RIPK3 in any given individual cell triggers either apoptosis or necroptosis and does not activate both pathways simultaneously. To explore this idea in more detail, we first defined IAV-infected cells undergoing apoptosis as those that were positive for both CC3 and the cell death marker SYTOX Green (CC3+SG+). These cells displayed classical features of apoptosis, including shrinkage and condensed chromatin (Fig. 2 C, middle panels). We next defined cells that were CC3− but SG+ as undergoing necroptosis; these cells typically had a swollen, balloon-like appearance (Fig. 2 C, bottom panels). Live cells were defined as CC3−SG− (Fig. 2 C, top panels). By these criteria, cells exposed to a canonical necroptosis stimulus (TNF + cycloheximide + zVAD-fmk; TCZ) expectedly underwent only necroptosis (green), whereas cells treated with a caspase-activating stimulus (TRAIL) succumbed primarily by apoptosis (red; Fig. 2 D). Intriguingly, roughly equal proportions of IAV-infected WT cells showed evidence of either apoptosis or necroptosis but rarely manifested signs of mixed apoptotic-necrotic death (black; Fig. 2 D). When RIPK3 kinase activity was blocked or when MLKL was absent, almost all dying cells showed apoptotic morphology (Fig. 2 D). In contrast, when caspase activity was prevented, or in *Casp8^DA* cells, cells died primarily by necroptosis (Fig. 2 D). Only when both RIPK3 kinase activity and caspase activity were inhibited, or in *Zbp1^−/−* MEFs, was cell death prevented. In agreement with these results, costaining WT MEFs for CC3 (apoptosis) and phosphorylated MLKL (pMLKL; necroptosis) showed that IAV-infected cells were either CC3+ (red arrows) or pMLKL+ (green arrows); again, cells double positive for CC3 and pMLKL were almost never seen (Fig. 2, E and F). As controls, cells were almost only pMLKL+ when treated with TCZ and primarily CC3+ when exposed to TRAIL (Fig. 2, E

and F). Over a time course of 12 h, the proportion of cells that were either CC3+ or pMLKL+ gradually increased to 40–50% of all infected (NP+) cells, but the ratio of CC3+ to pMLKL+ cells remained largely equivalent (Fig. 2 F). Notably, there was no significant difference between CC3+ and pMLKL+ cells in the intensity of the NP signal (Fig. S2 A), suggesting that the extent of virus replication may not be a major determinant of whether the cell undergoes apoptosis or necroptosis. In human HT-29 cells made competent for IAV-induced ZBP1/RIPK3-dependent cell death by stable expression of FLAG-ZBP1 (Fig. S2 B), IAV infection resulted in either necroptosis or apoptosis but not both outcomes (Fig. 2, G and H). IAV-infected cells in lung sections from WT mice were also either pMLKL+ or CC3+ but rarely both (Fig. 2, I and J). Interestingly, necroptosis appears to manifest notably earlier than apoptosis in HT-29 FLAG-ZBP1 cells (Fig. 2 H) and in infected lungs (Fig. 2 J). Taken together, these findings demonstrate that, although both apoptosis and necroptosis fates are theoretically available to RIPK3 in IAV-infected cells, only one of these two forms of death ultimately manifests.

Necroptosis can clear IAV from infected lungs in the absence of apoptosis

Following infection with IAV (2,500 50% egg infectious dose [EID_{50}]; ~LD_{20} for this virus in C57BL/6 mice), ~20% of WT mice succumbed by 12 d postinfection (d.p.i.); surviving mice made full recoveries (Fig. 3 A). *Mlkl^−/−* mice displayed survival and mortality rates that were mostly indistinguishable from those of WT mice in both kinetics and magnitude, demonstrating, as we have previously shown (Nogusa et al., 2016), that necroptosis is dispensable for preventing IAV-induced lethality in mice (Fig. 3 A). Importantly, >80% of *Casp8^DA* mice also survived this dose of IAV (Fig. 3 A); these mice made complete recoveries by 3 wk after infection. Only ~10% of *Casp8^DA Mlkl^−/−* mice, however, survived past 12 d.p.i. (Fig. 3 A). Comparing weights of infected *Casp8^DA* mice with those of *Casp8^DA Mlkl^−/−* mice showed that both genotypes initially lost weight with roughly equivalent kinetics, but whereas most *Casp8^DA* mice eventually rebounded to within 10% of their starting weights by 18 d.p.i., the majority of *Casp8^DA Mlkl^−/−* mice continued to lose weight and had to be killed by 12 d.p.i. (Fig. 3 B). *Casp8^DA* (and *Mlkl^−/−*) animals were able to control virus replication at least as effectively as WT mice at both early (3 and 5 d.p.i.; Fig. S2 C) and late (9 d.p.i.; Fig. 3 C) time points; indeed, lungs from *Casp8^DA* mice contained even lower levels of virus than lungs of either WT mice or *Mlkl^−/−* animals at 9 d.p.i. (Fig. 3 C), and IAV replication rates at early time points were modestly but significantly reduced in *Casp8^DA* MEFs compared with either WT or *Mlkl^−/−* cells (Fig. S2 D). In contrast, *Casp8^DA Mlkl^−/−* mice were unable to effectively curb IAV output and continued to support high levels of progeny virus production in their lungs late into infection (Fig. 3 C). These findings were corroborated by staining lung sections from each genotype for virus protein. Whereas only residual virus debris (black arrows) was observed in WT, *Casp8^DA*, and *Mlkl^−/−* mice at 9 d.p.i., similar sections from *Casp8^DA Mlkl^−/−* mice demonstrated persistence of virus in bronchiolar and alveolar epithelial cells (Fig. 3 D, red arrows). In agreement with these

Shubina et al.
Necroptosis is a stand-alone antiviral mechanism

Journal of Experimental Medicine   3 of 9
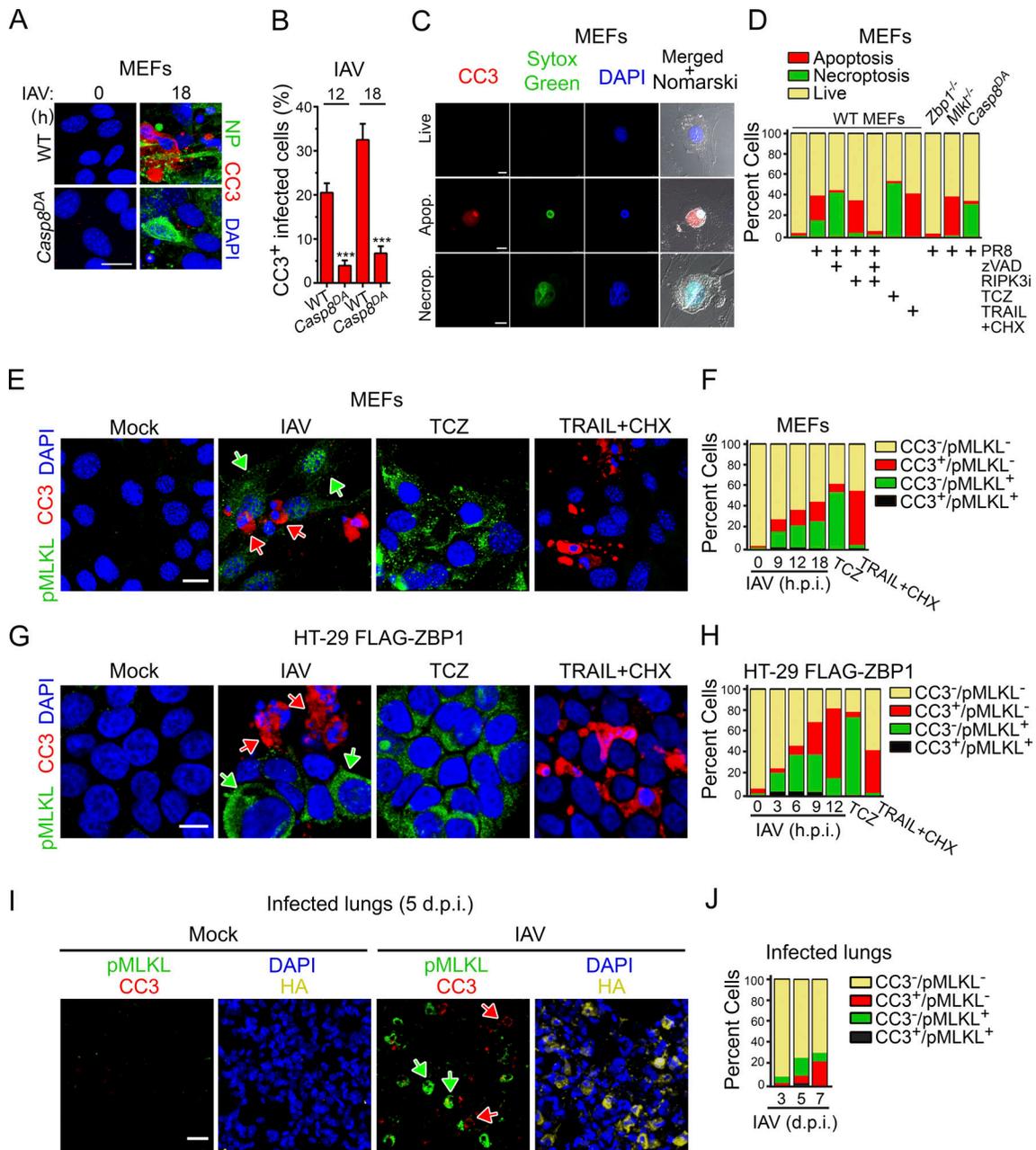https://doi.org/10.1084/jem.20191259

Figure 2. IAV-induced apoptosis and necroptosis do not occur in the same infected cell. (A) WT and *Casp8*[DA] MEFs infected with PR8 (MOI, 2) were examined for apoptosis using antibodies to CC3 (red) at 18 h.p.i. Virus replication was determined by staining for NP (green). Scale bar = 20 μm. **(B)** Quantification of CC3 in virus-positive infected cells at the indicated times after infection. Data are pooled from four fields with 30–60 cells/field; data are from one of four experiments with similar results. **(C)** MEFs were infected with PR8 (MOI, 2), harvested at 18 h.p.i., and stained for CC3 (red) and SYTOX Green. Scale bar = 10 μm. **(D)** Quantification of live, apoptotic, and necroptotic cells following the indicated treatments at 18 h (PR8; MOI, 2) or 12 h (TCZ, TRAIL + CHX). Data are pooled from four fields with 30–60 cells/field; data are from one of four experiments with similar results. **(E)** Primary MEFs infected with PR8 (MOI, 2; 18 h) or treated with either TCZ (12 h) or TRAIL + CHX (12 h) were examined for apoptosis and necroptosis by immunofluorescence using antibodies to CC3 (red) and pMLKL (green), respectively. Scale bar = 20 μm. **(F)** Quantification of CC3 and/or pMLKL positivity at the indicated times after infection (PR8) or at 12 h (TCZ, TRAIL + CHX). Data are pooled from four fields with 20–50 cells/field; data are from one of four experiments with similar results. **(G)** Human HT-29 cells made competent for IAV-activated cell death by stable retroviral expression of FLAG-tagged hZBP1 were infected with PR8 (MOI, 2; 9 h.p.i.) or treated with either TCZ (6 h) or TRAIL + CHX (9 h) and examined for apoptosis and necroptosis by immunofluorescence using antibodies to CC3 (red) and pMLKL (green). Scale bar = 10 μm. **(H)** Quantification of CC3 and/or pMLKL positivity at the indicated times after infection (PR8; MOI, 2). TCZ- and TRAIL + CHX–treated cells were evaluated at 6 h and 9 h after treatment, respectively. Data are pooled from four fields with 30–50 cells/field; data are from one of four experiments with similar results. **(I)** Mock- or IAV-infected lungs were stained for CC3 (red) or pMLKL (green) at 5 d.p.i. Nuclei are stained with DAPI (blue), and IAV HA is shown in yellow. Scale bar = 20 μm. **(J)** Quantification of pMLKL- and CC3-positive cells in IAV-infected lungs at the indicated days after infection. Arrows in E, G, and I point to pMLKL[+] (green) or CC3^{+} (red) cells. Data are pooled from seven fields with 60–130 cells/field; data are from one of two experiments with similar results. Unpaired Student's *t* test (B). Error bars represent mean ± SD. ***, P < 0.005.
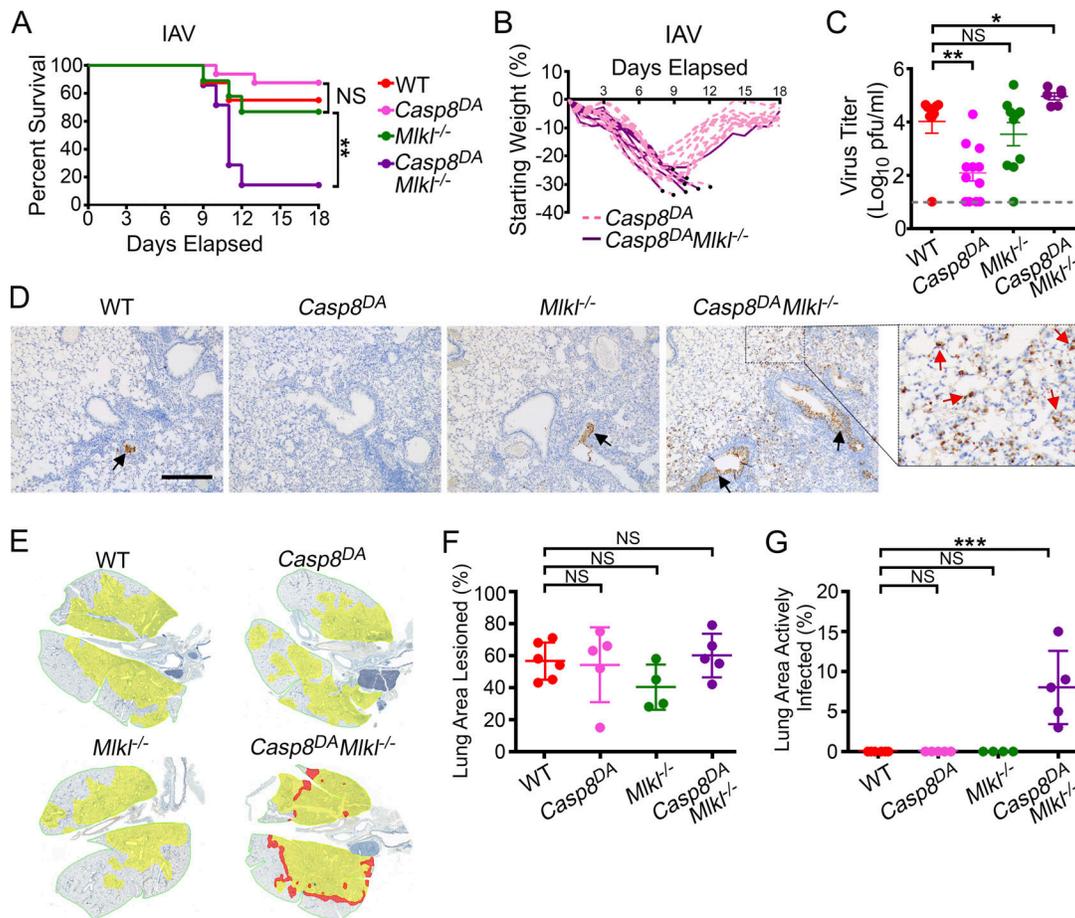
Figure 3. **Necroptosis protects against IAV in the absence of apoptosis. (A)** Survival analysis of 8–12-wk-old sex-matched mice of the indicated genotypes (WT, $n = 8$; $Casp8^{DA}$, $n = 13$; $Mlkl^{-/-}$, $n = 7$; $Casp8^{DA}Mlkl^{-/-}$, $n = 7$) following infection with PR8 (2,500 EID$_{50}$/mouse). **(B)** Weight loss analysis of $Casp8^{DA}$ and $Casp8^{DA}Mlkl^{-/-}$ mice shown in A. Dead mice are represented by black circles. $Casp8^{DA}$, $n = 13$; $Casp8^{DA}Mlkl^{-/-}$, $n = 7$. **(C)** Lung virus titers of mice of the indicated genotypes at 9 d.p.i. with PR8 (1,500 EID$_{50}$). WT, $n = 8$; $Casp8^{DA}$, $n = 12$; $Mlkl^{-/-}$, $n = 10$; $Casp8^{DA}Mlkl^{-/-}$, $n = 6$. **(D)** Staining for IAV antigen in the lung at 9 d.p.i. with PR8 (1,500 EID$_{50}$). Red arrows show actively infected cells in lungs of $Casp8^{DA}Mlkl^{-/-}$ mice. Black arrows point to antigen-positive extracellular virus debris. Scale bar = 300 μm. **(E)** Morphometry of virus spread. Alveolar areas containing virus antigen–positive cells are highlighted in red, and lesioned areas with no/minimal antigen-positive debris are shown in yellow. **(F)** Percentage of infected lungs with lesioned areas, calculated from the morphometric images shown in E. WT, $n = 6$; $Casp8^{DA}$, $n = 5$; $Mlkl^{-/-}$, $n = 4$; $Casp8^{DA}Mlkl^{-/-}$, $n = 5$. **(G)** Percentage of infected lung showing areas of active infection, calculated from the morphometric images shown in E. WT, $n = 6$; $Casp8^{DA}$, $n = 5$; $Mlkl^{-/-}$, $n = 4$; $Casp8^{DA}Mlkl^{-/-}$, $n = 5$. Data are representative of (A and B) or pooled from (C–G) two independent experiments. Log-rank (Mantel-Cox) test (A); Mann-Whitney test (C); one-way ANOVA comparing WT samples with every other genotype (G and H). Error bars represent mean ± SD. *, $P < 0.05$; **, $P < 0.005$; ***, $P < 0.00005$.

findings, $Casp8^{DA}Mlkl^{-/-}$ mice at 9 d.p.i. displayed clear zones of ongoing virus replication (red) in cells along the entire periphery of the lesioned lung (yellow), whereas both $Casp8^{DA}$ and $Mlkl^{-/-}$ mice, like their WT counterparts, showed no evidence of active virus replication by this time point (Fig. 3 E, quantified in Fig. 3, F and G). Collectively, these data also demonstrate that necroptosis on its own can protect against IAV and, in fact, may represent a more efficient means of viral clearance than apoptosis alone.

Necroptosis by itself can mediate effective anti-IAV adaptive immune responses

Lung sections from $Casp8^{DA}$ mice were overtly similar to those of WT control animals (and to $Mlkl^{-/-}$ mice) when evaluated for classical indicators of IAV-mediated pathology (e.g., presence of hyaline membranes, septal thickening, and inflamed alveoli),

whereas similar sections from $Casp8^{DA}Mlkl^{-/-}$ mice showed markedly increased evidence of inflammatory injury, including significantly elevated levels of alveolar inflammation (Fig. 4 A), compared with any of the other genotypes. These observations are consistent with increased virus replication in $Casp8^{DA}Mlkl^{-/-}$ lungs and reminiscent of our previous results in $Ripk3^{-/-}$ mice (Nogusa et al., 2016). Notably, our earlier work also showed that $Ripk3^{-/-}$ mice failed to mount effective CD8$^+$ T cell–driven adaptive immune responses to IAV (Nogusa et al., 2016). To examine if $Casp8^{DA}$ mice were similarly compromised in their CD8$^+$ T cell responses, we first evaluated the location and abundance of lymphoid cells in infected lungs. $Casp8^{DA}$ mice displayed numbers and distribution of lymphoid cells that were mostly indistinguishable from those of WT or $Mlkl^{-/-}$ mice on the basis of H&E staining (Fig. 4 B). Compared with the other genotypes, however, $Casp8^{DA}Mlkl^{-/-}$ mice had markedly
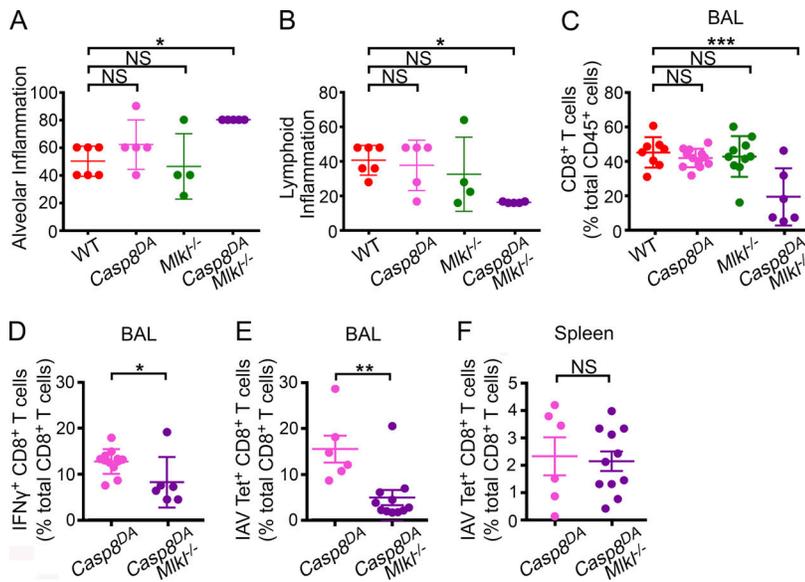
Figure 4. **Necroptosis mediates effective anti-IAV CD8+ T cell responses in the absence of apoptosis. (A)** Quantification of alveolar inflammation in infected lungs from mice of the indicated genotypes at 6 d.p.i. with PR8 (1,500 EID$_{50}$). WT, n = 6; $Casp8^{DA}$, n = 5; $Mlkl^{-/-}$, n = 4; $Casp8^{DA}Mlkl^{-/-}$, n = 5. **(B)** Assessment of lymphoid inflammation from infected lungs of the indicated genotypes at 6 d.p.i. with PR8 (1,500 EID$_{50}$). WT, n = 6; $Casp8^{DA}$, n = 5; $Mlkl^{-/-}$, n = 4; $Casp8^{DA}Mlkl^{-/-}$, n = 5. **(C)** Percentage of CD8+ T cells as a proportion of all immune (CD45+) cells in the BAL of mice of the indicated genotypes at 9 d.p.i. with PR8 (1,500 EID$_{50}$). WT, n = 8; $Casp8^{DA}$, n = 12; $Mlkl^{-/-}$, n = 10; $Casp8^{DA}Mlkl^{-/-}$, n = 6. **(D)** Frequencies of IFNγ+ CD8+ T cells among all CD8+ T cells from the BAL of mice of the indicated genotypes following stimulation with IAV PB1$_{703-711}$ peptide ex vivo. BAL fluid was collected at 8 d.p.i. with PR8 (1,500 EID$_{50}$). $Casp8^{DA}$, n = 12; $Casp8^{DA}Mlkl^{-/-}$, n = 6. **(E)** Frequencies of IAV PB1$_{703-711}$ tetramer+ CD8+ T cells from the BAL of mice of the indicated genotypes collected at 8 d.p.i. with PR8 (1,500 EID$_{50}$). $Casp8^{DA}$, n = 6; $Casp8^{DA}Mlkl^{-/-}$, n = 11. **(F)** Frequencies of IAV PB1$_{703-711}$ tetramer+ CD8+ T cells from the spleens of mice of the indicated genotypes collected at 8 d.p.i. with PR8 (1,500 EID$_{50}$). $Casp8^{DA}$, n = 6; $Casp8^{DA}Mlkl^{-/-}$, n = 11. Gating strategy used for flow cytometric analyses in this figure is shown in Fig. S3 D. Data are pooled from two independent experiments (A–F). One-way ANOVA comparing WT samples with every other genotype (A–F). Error bars represent mean ± SD. *, P < 0.05; **, P < 0.005; ***, P < 0.0005.

diminished evidence of lymphoid inflammation (both T and B cells; Fig. 4 B). When we examined bronchoalveolar lavage (BAL) fluid from IAV-infected mice of each genotype, we found that $Casp8^{DA}$ mice displayed frequencies of CD8+ T cells that were equivalent to those of WT animals (Fig. 4 C), whereas $Casp8^{DA}Mlkl^{-/-}$ mice had a significantly lower proportion (among immune cells) of CD8+ T cells than any of the other genotypes (Fig. 4 C). Following stimulation with IAV-specific peptides ex vivo, $Casp8^{DA}$ mice mounted anti-IAV CD8+ T cell responses that were indistinguishable from those of WT mice, while $Casp8^{DA}Mlkl^{-/-}$ mice had significantly lower numbers of IFNγ-producing, IAV-specific CD8+ T cells as compared with $Casp8^{DA}$ mice (Fig. 4 D), paralleling our results from $Ripk3^{-/-}$ mice (Nogusa et al., 2016). Of note, activation of CD8+ T cells by a nonspecific stimulus (PMA/ionomycin) ex vivo was not dampened in $Casp8^{DA}Mlkl^{-/-}$ mice, demonstrating that $Casp8^{DA}Mlkl^{-/-}$ CD8+ T cells are not intrinsically encumbered in their capacity to survive and proliferate once activated (Fig. S3 A). Moreover, whereas $Casp8^{DA}Mlkl^{-/-}$ mice showed significantly lower frequencies (Fig. 4 E) and numbers (Fig. S3 B) of IAV-specific CD8+ T cells in BAL fluid, the frequencies (Fig. 4 F) and numbers (Fig. S3 C) of these cells were not diminished in the spleen compared with $Casp8^{DA}$ mice. Altogether, these results show that apoptosis is not required for effective anti-IAV CD8+ T cell responses in pulmonary tissue, as long as necroptosis signaling is intact. They also demonstrate that necroptosis is a bona fide stand-alone antiviral mechanism in vivo.

The idea that necroptosis is a "backup" fail-safe cell death mechanism secondary to apoptosis emerged from studies with the cytokine TNF-α, where inactivation of apoptosis signals is a prerequisite for licensing necroptosis, and from work with

murine CMV, which encodes an inhibitor of Casp8-dependent apoptosis (Mocarski et al., 2014; Moriwaki and Chan, 2013; Upton et al., 2010, 2017). The substantial number of viruses encoding Casp8 inhibitors suggests that necroptosis might have evolved as a counteradaptation to eliminate cells with compromised apoptosis signaling (Mocarski et al., 2011). Using the $Casp8^{DA}$ mouse, we now show that necroptosis can fully compensate for the absence of apoptosis to efficiently limit virus spread, mobilize adaptive immunity, and ultimately clear the virus (in this case, IAV) from the host.

It is noteworthy that necroptosis appears to peak earlier than apoptosis in vivo (Fig. 2 J), and viral titers were statistically lower in $Casp8^{DA}$ mice at 9 d.p.i. than in $Mlkl^{-/-}$ mice or WT controls (Fig. 3 C). These findings suggest that necroptosis may in fact be a more efficient means of controlling IAV than apoptosis, perhaps by virtue of its earlier deployment during the host anti-IAV response. Interestingly, the rates of IAV RNA synthesis were moderately reduced in $Casp8^{DA}$ MEFs compared with either $Mlkl^{-/-}$ or WT MEFs (Fig. S2 D), although the kinetics of IAV-triggered cell death were largely similar between all three genotypes (Fig. 1 F), indicating that triggering the necroptosis machinery in the absence of apoptosis signaling may limit virus replication even before the cell dies.

IAV is the first physiological stimulus, to our knowledge, that activates both apoptosis and necroptosis in parallel downstream of RIPK3 (Nogusa et al., 2016). These observations raise the question of how RIPK3, at the single-cell level, "decides" between apoptosis and necroptosis. Is the decision to trigger either cell fate a stochastic one, in which both outcomes are equally probable and determined simply by levels of downstream effectors (i.e., RIPK1 for apoptosis and MLKL for necroptosis) in

the vicinity of activated RIPK3 (Cook et al., 2014)? Or is cell death downstream of RIPK3 governed by active mechanisms (such as post-translational modifications of RIPK3 and/or its effectors) that determine whether the individual cell dies by apoptosis or by necroptosis? Our finding that IAV-infected cells positive for phosphorylated MLKL are almost always negative for activated effector caspases, and vice versa, strongly suggests that once a cell commits to a form of death, the other fate becomes unavailable. That is, although the "decision" at the level of activated RIPK3 to trigger apoptosis or necroptosis might be stochastic, once this decision is made, active mechanisms are likely invoked to prevent parallel triggering of the other death modality. An initial stochastic "choice" of a particular fate, followed by active suppression of the alternative death pathway, supplies a compelling explanation for why cells positive for phosphorylated MLKL or active Casp3 are found in roughly equal proportions, but cells positive for both signals, or cells undergoing death with morphological features of both apoptosis and necroptosis, are rarely observed. Regulated ubiquitylation of ZBP1, RIPK3, and/or downstream proteins may be an attractive mechanistic explanation for how this cell fate switch might be controlled (Dondelinger et al., 2016; Kesavardhana et al., 2017; Rodrigue-Gervais et al., 2014; Seo et al., 2016; Witt and Vucic, 2017).

Materials and methods

Mice and cells
Mice were housed in specific pathogen–free facilities at the Fox Chase Cancer Center and at St. Jude Children's Research Hospital, and all in vivo experiments were conducted under protocols approved by the Committees on Use and Care of Animals at these institutions. MEFs were generated from embryonic day 14.5 embryos and used within five passages in experiments. All strains were backcrossed at least nine times onto a C57BL/6 background. WT littermate controls or WT C57BL/6 mice (The Jackson Laboratory) were used as controls. $Mlkl^{-/-}$ mice have been described before (Murphy et al., 2013). $Casp8^{DA}$ mice were generated in-house (Fig. S1).

Reagents
Biological and chemical reagents were obtained from the following sources: zVAD.fmk (Bachem), mTNF-α and mTRAIL (R&D Systems), RIPK3 inhibitors GSK'843 (GlaxoSmithKline), Live/Dead Aqua and Ghost Violet 510 dyes (Tonbo Biosciences), and SYTOX Green (Thermo Fisher Scientific). Primary antibodies to β-actin (Sigma-Aldrich), total Casp8, CC8, total Casp3, CC3 (Cell Signaling Technology), FADD (EMD Millipore), IAV hemagglutinin (HA) (Sigma-Aldrich), IAV NP (Bio-Rad Laboratories), IAV NS1 (Santa Cruz Biotechnology), IAV H1N1 (strain USSR; United States Biological), MLKL (EMD Millipore), phospho-murine MLKL for immunoblotting (Cell Signaling Technology), phospho-human MLKL (MyBioSource), RIPK1 (BD Transduction Laboratories), ZBP1 (AdipoGen Life Sciences), and RIPK3 (ProSci) were obtained from the indicated commercial sources. Antibodies to phospho-murine MLKL for use in immunofluorescence studies have been described before (Rodriguez et al., 2016). Primary fluorophore-conjugated

antibodies for FACS analysis were obtained from BioLegend, except for PE/cyanine 7 (Cy7)-conjugated IFN-γ (BD PharMingen) and V450-conjugated CD45 (Tonbo Biosciences). Secondary fluorophore-conjugated antibodies for immunofluorescence microscopy were procured from Thermo Fisher Scientific. IAV-specific H-2K^b class I MHC tetramers loaded with PB1$_{703-711}$ peptides were generated by the Immune Monitoring Core at the Fred Hutchinson Cancer Research Center. IAV strain A/Puerto Rico/8/1934 (PR8, H1N1) was propagated by allantoic inoculation of embryonated hen eggs with diluted (1:10^6) seed virus. Stock virus titers were determined as EID$_{50}$.

Virus infection and titration
Age-matched (8–12-wk-old) and sex-matched mice were anesthetized with Avertin (2,2,2-tribromoethanol; Winthrop Laboratories) or isoflurane and infected intranasally with virus inoculum diluted in endotoxin-free saline. Mice were either monitored for survival and weight loss over a period of 18 d or sacrificed at defined time points for analysis of histology and virus replication. Mice losing >35% body weight were considered moribund and euthanized by CO$_2$ asphyxiation. For cell culture experiments, near-confluent monolayers of cells were infected with virus in serum-free DMEM for 1 h, with occasional gentle rocking, in a humidified tissue culture incubator maintained at 37°C and 5% CO$_2$. Following infection, the inoculum was removed and replaced with growth medium. In conditions involving small-molecule inhibitors, cells were preincubated for 1 h with inhibitors before infection; after removal of inoculum and washing, inhibitors were added back to the medium. Cell viability was determined by Trypan Blue exclusion or SYTOX Green uptake. Titration of virus was conducted by standard plaque assay of diluted lung homogenates on monolayers of Madin-Darby canine kidney cells. Plaques were scored after 3 d of incubation.

Quantitative PCR
Total RNA from IAV-infected cells was isolated and purified using the NucleoSpin RNA isolation kit (MACHEREY-NAGEL). RNA was reverse transcribed into cDNA using SuperScript IV VILO Master Mix (Thermo Fisher Scientific). Quantitative PCR was performed to detect polymerase acidic protein (PA) defective viral genomes using SYBR Green (Thermo Fisher Scientific) and the following primers: PA-(forward) 5′-GCTTCTTATCGT TCAGGCTCTT-3′; PA-(reverse) 5′-GGGATCATTAATCAGGCA CTCC-3′.

Fluorescence microscopy
Cells were plated on 8-well glass slides (EMD Millipore) and allowed to adhere for at least 24 h before use in experiments. Following treatment or virus infection, cells were fixed, stained, and imaged as previously described (Zhang et al., 2020). For immunofluorescence studies on lung sections, lungs were fixed by intratracheal perfusion and subsequent immersion in freshly prepared 4% paraformaldehyde for 24 h. Fixed lungs were then immersed in 30% sucrose, embedded in optimal cutting temperature compound (Thermo Fisher Scientific), frozen, and sectioned. Frozen sections were stained and imaged as described previously (Zhang et al., 2020). In some experiments, cells were

incubated with SYTOX Green for 15 min before fixation. Primary antibodies were diluted as follows: anti-CC3, 1:200; anti-NP, 1:1,000; anti-HA, 1:500; anti-pMLKL (murine), 1:10,000; and anti-pMLKL (human), 1:200.

Histology and morphometry

Lungs from IAV-infected mice were fixed via intratracheal infusion and subsequent immersion in freshly prepared 4% paraformaldehyde. Tissues were paraffin embedded, sectioned, and stained for virus with anti-IAV H1N1 antibody (1:1,000) and a secondary biotinylated donkey antigoat antibody (Santa Cruz Biotechnology; 1:200 on tissue sections subjected to antigen retrieval for 30 min at 98°C). The extent of virus spread was quantified by first capturing digital images of whole-lung sections stained for viral antigen by using an Aperio ScanScope XT Slide Scanner (Aperio Technologies), then manually outlining fields with the alveolar areas containing virus antigen–positive pneumocytes highlighted in red (defined as "active" infection), whereas lesioned areas containing no antigen-positive cells and no/minimal antigen-positive debris were highlighted in yellow (defined as "inactive" infection). The percentage of each lung field with infection/lesions was calculated using the Aperio ImageScope software. The extent and severity of pulmonary inflammation were determined from blinded sections examined by a pathologist and scored on a severity scale as follows: 0 = no lesions; 1 = minimal, focal to multifocal, barely detectable; 15 = mild, multifocal, small but conspicuous; 40 = moderate, multifocal, prominent; 80 = marked, multifocal coalescing, lobar; 100 = severe, diffuse, with extensive disruption of normal architecture and function. These scores were converted to a semiquantitative scale as described previously (Matute-Bello et al., 2011).

CD8+ T cell responses

BAL fluid was collected by inserting a catheter into the trachea and washing with 3 × 1 ml of 1× PBS. Cells from BAL fluid or spleens were pelleted by centrifuging at 1,500 rpm for 5 min. RBC lysis was performed, cells were washed with HBSS, and counted using a Vi-CELL XR cell counter (Beckman Coulter). For ex vivo stimulation and intracellular cytokine staining, 10^6 total lung cells were plated in a 96-well plate for each condition. Cells were stimulated with Cell Stimulation Cocktail (BioLegend), containing PMA/ionomycin and Brefeldin A, at a dilution of 1:500 or with IAV peptides at a concentration of 1 μM for 4 h. Following stimulation, cells were washed and then incubated with Fc block at a dilution of 1:100 for 10 min at room temperature. For surface staining, cells were washed and incubated in 100 μl of FACS buffer (1% FBS/1 mM EDTA in 1× PBS) containing Live/Dead Aqua dye (1:100), allophycocyanin (APC)/Cy7-conjugated antimouse CD45 (1:100), PE-conjugated antimouse CD3 (1:100), APC-conjugated antimouse CD8 (1:200), and FITC-conjugated antimouse CD4 (1:200) for 30 min at room temperature. For intracellular staining, cells were fixed and membranes permeabilized by incubating in 100 μl of fixation/permeabilization solution (BD Biosciences) for 20 min on ice. Cells were washed with permeabilization buffer and then incubated with PE/Cy7-conjugated antimouse IFN-γ (1:100) for 30 min on ice. Following intracellular staining, cells were washed twice

with FACS buffer, resuspended in 100 μl of FACS buffer, and analyzed on a BD LSR Fortessa Cell Analyzer (BD Biosciences). For tetramer staining, cells were incubated with Fc block (1:100; BioLegend) at room temperature, washed, and incubated with IAV peptide:MHC tetramers conjugated to PE. Cells were incubated with tetramers for 1 h on ice and washed twice with FACS buffer. Following tetramer staining, cells were stained with the following antibodies and dyes on ice for 30 min: Ghost Dye Violet 510 (1:100), CD45-V450 (1:100), CD3-BV785 (1:100), CD8-BV650 (1:200), and CD4-APC Fire 750 (1:200). Cells were washed twice in FACS buffer, resuspended in 100 μl of FACS buffer, and analyzed on a BD LSR Fortessa Cell Analyzer.

Online supplemental material

Fig. S1 describes the generation and characterization of the Casp8DA mouse. Fig. S2 provides additional information on the influence of IAV replication rates on cell death outcomes (and vice versa) and demonstrates that ZBP1-expressing HT-29 cells support IAV-activated death signaling. Fig. S3 provides additional characterization of CD8+ T cell responses in mice lacking apoptosis and/or necroptosis signaling and outlines the gating strategy used to evaluate these and other immunological parameters by flow cytometry.

References

Ashkenazi, A., and V.M. Dixit. 1998. Death receptors: signaling and modulation. *Science*. 281:1305–1308. https://doi.org/10.1126/science.281.5381.1305

Cook, W.D., D.M. Moujalled, T.J. Ralph, P. Lock, S.N. Young, J.M. Murphy, and D.L. Vaux. 2014. RIPK1- and RIPK3-induced cell death mode is determined by target availability. *Cell Death Differ*. 21:1600–1612. https://doi.org/10.1038/cdd.2014.70

Daniels, B.P., A.G. Snyder, T.M. Olsen, S. Orozco, T.H. Oguin, III, S.W.G. Tait, J. Martinez, M. Gale, Jr., Y.M. Loo, and A. Oberst. 2017. RIPK3 restricts viral pathogenesis via cell death-independent neuroinflammation. *Cell*. 169:301–313.e11. https://doi.org/10.1016/j.cell.2017.03.011

Daniels, B.P., S.B. Kofman, J.R. Smith, G.T. Norris, A.G. Snyder, J.P. Kolb, X. Gao, J.W. Locasale, J. Martinez, M. Gale, Jr., et al. 2019. The nucleotide sensor ZBP1 and kinase RIPK3 induce the enzyme IRG1 to promote an antiviral metabolic state in neurons. *Immunity*. 50:64–76.e4. https://doi.org/10.1016/j.immuni.2018.11.017

Dillon, C.P., A. Oberst, R. Weinlich, L.J. Janke, T.B. Kang, T. Ben-Moshe, T.W. Mak, D. Wallach, and D.R. Green. 2012. Survival function of the FADD-CASPASE-8-cFLIP(L) complex. *Cell Rep*. 1:401–407. https://doi.org/10.1016/j.celrep.2012.03.010

Dillon, C.P., B. Tummers, K. Baran, and D.R. Green. 2016. Developmental checkpoints guarded by regulated necrosis. *Cell. Mol. Life Sci*. 73:2125–2136. https://doi.org/10.1007/s00018-016-2188-z

Dondelinger, Y., M. Darding, M.J. Bertrand, and H. Walczak. 2016. Polyubiquitination in TNFR1-mediated necroptosis. *Cell. Mol. Life Sci*. 73:2165–2176. https://doi.org/10.1007/s00018-016-2191-4

Harris, K.G., S.A. Morosky, C.G. Drummond, M. Patel, C. Kim, D.B. Stolz, J.M. Bergelson, S. Cherry, and C.B. Coyne. 2015. RIP3 regulates autophagy and promotes coxsackievirus B3 infection of intestinal epithelial cells. *Cell Host Microbe*. 18:221–232. https://doi.org/10.1016/j.chom.2015.07.007

Herold, S., S. Ludwig, S. Pleschka, and T. Wolff. 2012. Apoptosis signaling in influenza virus propagation, innate host defense, and lung injury. *J. Leukoc. Biol*. 92:75–82. https://doi.org/10.1189/jlb.1011530

Kang, T.B., G.S. Oh, E. Scandella, B. Bolinger, B. Ludewig, A. Kovalenko, and D. Wallach. 2008. Mutation of a self-processing site in caspase-8 compromises its apoptotic but not its nonapoptotic functions in bacterial artificial chromosome-transgenic mice. *J. Immunol*. 181:2522–2532. https://doi.org/10.4049/jimmunol.181.4.2522

Kesavardhana, S., T. Kuriakose, C.S. Guy, P. Samir, R.K.S. Malireddi, A. Mishra, and T.D. Kanneganti. 2017. ZBP1/DAI ubiquitination and sensing of influenza vRNPs activate programmed cell death. *J. Exp. Med*. 214:2217–2229. https://doi.org/10.1084/jem.20170550

Kuriakose, T., S.M. Man, R.K.S. Malireddi, R. Karki, S. Kesavardhana, D.E. Place, G. Neale, P. Vogel, and T.-D. Kanneganti. 2016. ZBP1/DAI is an innate sensor of influenza virus triggering the NLRP3 inflammasome and programmed cell death pathways. *Sci. Immunol*. 1. aag2045. https://doi.org/10.1126/sciimmunol.aag2045

Mandal, P., S.B. Berger, S. Pillay, K. Moriwaki, C. Huang, H. Guo, J.D. Lich, J. Finger, V. Kasparcova, B. Votta, et al. 2014. RIP3 induces apoptosis independent of pronecrotic kinase activity. *Mol. Cell*. 56:481–495. https://doi.org/10.1016/j.molcel.2014.10.021

Matute-Bello, G., G. Downey, B.B. Moore, S.D. Groshong, M.A. Matthay, A.S. Slutsky, and W.M. Kuebler; Acute Lung Injury in Animals Study Group. 2011. An official American Thoracic Society workshop report: features and measurements of experimental acute lung injury in animals. *Am J Respir Cell Mol Biol*. 44:725–738.

Mocarski, E.S., J.W. Upton, and W.J. Kaiser. 2011. Viral infection and the evolution of caspase 8-regulated apoptotic and necrotic death pathways. *Nat. Rev. Immunol*. 12:79–88. https://doi.org/10.1038/nri3131

Mocarski, E.S., W.J. Kaiser, D. Livingston-Rosanoff, J.W. Upton, and L.P. Daley-Bauer. 2014. True grit: programmed necrosis in antiviral host defense, inflammation, and immunogenicity. *J. Immunol*. 192:2019–2026. https://doi.org/10.4049/jimmunol.1302426

Moriwaki, K., and F.K. Chan. 2013. RIP3: a molecular switch for necrosis and inflammation. *Genes Dev*. 27:1640–1649. https://doi.org/10.1101/gad.223321.113

Murphy, J.M., P.E. Czabotar, J.M. Hildebrand, I.S. Lucet, J.G. Zhang, S. Alvarez-Diaz, R. Lewis, N. Lalaoui, D. Metcalf, A.I. Webb, et al. 2013. The pseudokinase MLKL mediates necroptosis via a molecular switch mechanism. *Immunity*. 39:443–453. https://doi.org/10.1016/j.immuni.2013.06.018

Nogusa, S., R.J. Thapa, C.P. Dillon, S. Liedmann, T.H. Oguin, III, J.P. Ingram, D.A. Rodriguez, R. Kosoff, S. Sharma, O. Sturm, et al. 2016. RIPK3 activates parallel pathways of MLKL-driven necroptosis and FADD-mediated apoptosis to protect against influenza A virus. *Cell Host Microbe*. 20:13–24. https://doi.org/10.1016/j.chom.2016.05.011

Oberst, A., C.P. Dillon, R. Weinlich, L.L. McCormick, P. Fitzgerald, C. Pop, R. Hakem, G.S. Salvesen, and D.R. Green. 2011. Catalytic activity of the caspase-8-FLIP(L) complex inhibits RIPK3-dependent necrosis. *Nature*. 471:363–367. https://doi.org/10.1038/nature09852

Philip, N.H., A. DeLaney, L.W. Peterson, M. Santos-Marrero, J.T. Grier, Y. Sun, M.A. Wynosky-Dolfi, E.E. Zwack, B. Hu, T.M. Olsen, et al. 2016. Activity of uncleaved caspase-8 controls anti-bacterial immune defense and TLR-induced cytokine production independent of cell death. *PLoS Pathog*. 12. e1005910. https://doi.org/10.1371/journal.ppat.1005910

Rodrigue-Gervais, I.G., K. Labbé, M. Dagenais, J. Dupaul-Chicoine, C. Champagne, A. Morizot, A. Skeldon, E.L. Brincks, S.M. Vidal, T.S. Griffith, et al. 2014. Cellular inhibitor of apoptosis protein cIAP2 protects against pulmonary tissue necrosis during influenza virus infection to promote host survival. *Cell Host Microbe*. 15:23–35. https://doi.org/10.1016/j.chom.2013.12.003

Rodriguez, D.A., R. Weinlich, S. Brown, C. Guy, P. Fitzgerald, C.P. Dillon, A. Oberst, G. Quarato, J. Low, J.G. Cripps, et al. 2016. Characterization of RIPK3-mediated phosphorylation of the activation loop of MLKL during necroptosis. *Cell Death Differ*. 23:76–88. https://doi.org/10.1038/cdd.2015.70

Sai, K., C. Parsons, J.S. House, S. Kathariou, and J. Ninomiya-Tsuji. 2019. Necroptosis mediators RIPK3 and MLKL suppress intracellular *Listeria* replication independently of host cell killing. *J. Cell Biol*. 218:1994–2005. https://doi.org/10.1083/jcb.201810014

Seo, J., E.W. Lee, H. Sung, D. Seong, Y. Dondelinger, J. Shin, M. Jeong, H.K. Lee, J.H. Kim, S.Y. Han, et al. 2016. CHIP controls necroptosis through ubiquitylation- and lysosome-dependent degradation of RIPK3. *Nat. Cell Biol*. 18:291–302. https://doi.org/10.1038/ncb3314

Thapa, R.J., J.P. Ingram, K.B. Ragan, S. Nogusa, D.F. Boyd, A.A. Benitez, H. Sridharan, R. Kosoff, M. Shubina, V.J. Landsteiner, et al. 2016. DAI senses influenza A virus genomic RNA and activates RIPK3-dependent cell death. *Cell Host Microbe*. 20:674–681. https://doi.org/10.1016/j.chom.2016.09.014

Tummers, B., L. Mari, C.S. Guy, B.L. Heckmann, D.A. Rodriguez, S. Rühl, J. Moretti, J.C. Crawford, P. Fitzgerald, T.D. Kanneganti, et al. 2020. Caspase-8-dependent inflammatory responses are controlled by its adaptor, FADD, and necroptosis. *Immunity*. 52:994–1006.e8. https://doi.org/10.1016/j.immuni.2020.04.010

Upton, J.W., W.J. Kaiser, and E.S. Mocarski. 2010. Virus inhibition of RIP3-dependent necrosis. *Cell Host Microbe*. 7:302–313. https://doi.org/10.1016/j.chom.2010.03.006

Upton, J.W., M. Shubina, and S. Balachandran. 2017. RIPK3-driven cell death during virus infections. *Immunol. Rev*. 277:90–101. https://doi.org/10.1111/imr.12539

Vanden Berghe, T., B. Hassannia, and P. Vandenabeele. 2016. An outline of necrosome triggers. *Cell. Mol. Life Sci*. 73:2137–2152. https://doi.org/10.1007/s00018-016-2189-y

Witt, A., and D. Vucic. 2017. Diverse ubiquitin linkages regulate RIP kinases-mediated inflammatory and cell death signaling. *Cell Death Differ*. 24:1160–1171. https://doi.org/10.1038/cdd.2017.33

Zhang, T., C. Yin, D.F. Boyd, G. Quarato, J.P. Ingram, M. Shubina, K.B. Ragan, T. Ishizuka, J.C. Crawford, B. Tummers, et al. 2020. Influenza virus Z-RNAs induce ZBP1-mediated necroptosis. *Cell*. 180:1115–1129.e13. https://doi.org/10.1016/j.cell.2020.02.050

A

Fwd primer

Casp8^{DA} allele

5'-TACCAAAGCGCAGACCACAA

D387A

TACCAAAGCGCAGACCACAA.........ACAGAACCACACTTTGGAGGTT GCG AGCTCATCT.........TGGCAAAGTGGGAGAGATGG

ACCGTTTCACCCTCTCTACC-5'

Rev primer

*Sac*I cleavage site

Amplicon size: 610 bp
After *Sac*I cleavage: WT/WT: 610 bp
WT/DA: 610, 410, & 200 bp
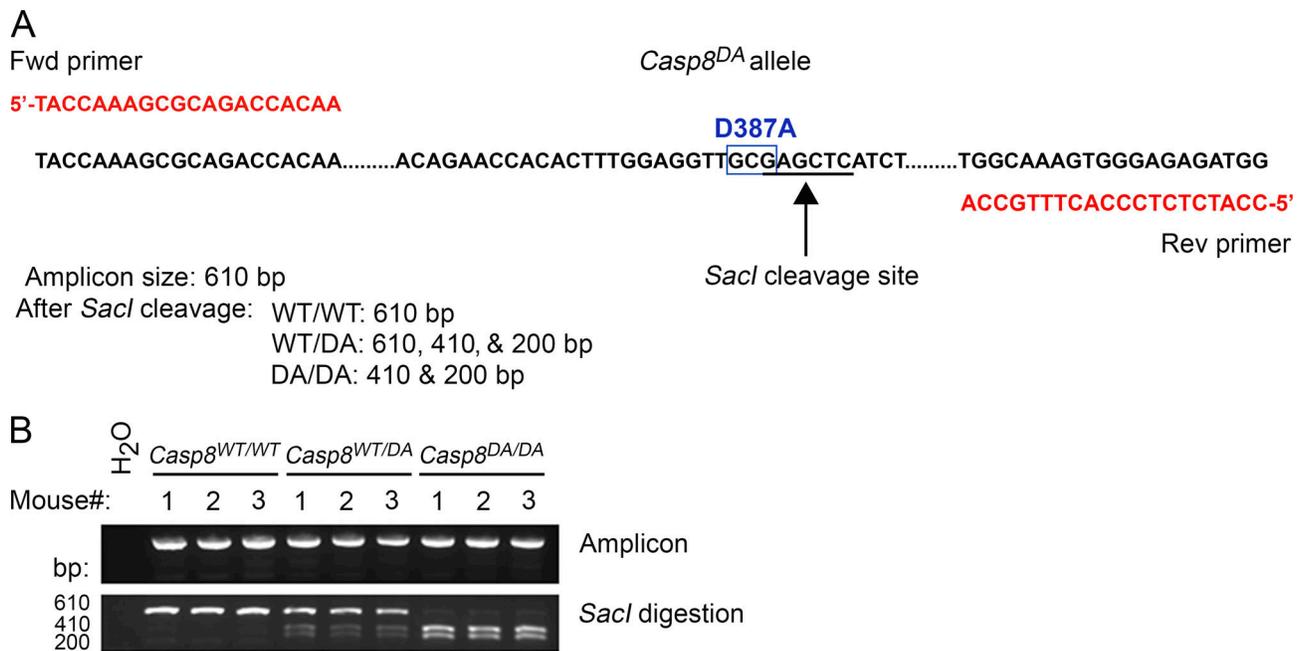DA/DA: 410 & 200 bp

B

Figure S1. **Generation of *Casp8^{DA}* mice. (A)** Schematic of the *Casp8^{DA}* allele showing primer sequences, location of the SacI cleavage site, and sizes of expected PCR amplicons after cleavage with SacI. **(B)** PCR results showing undigested (top) or SacI-digested (bottom) amplicon products produced from genomic tail DNA of mice from the indicated genotypes.
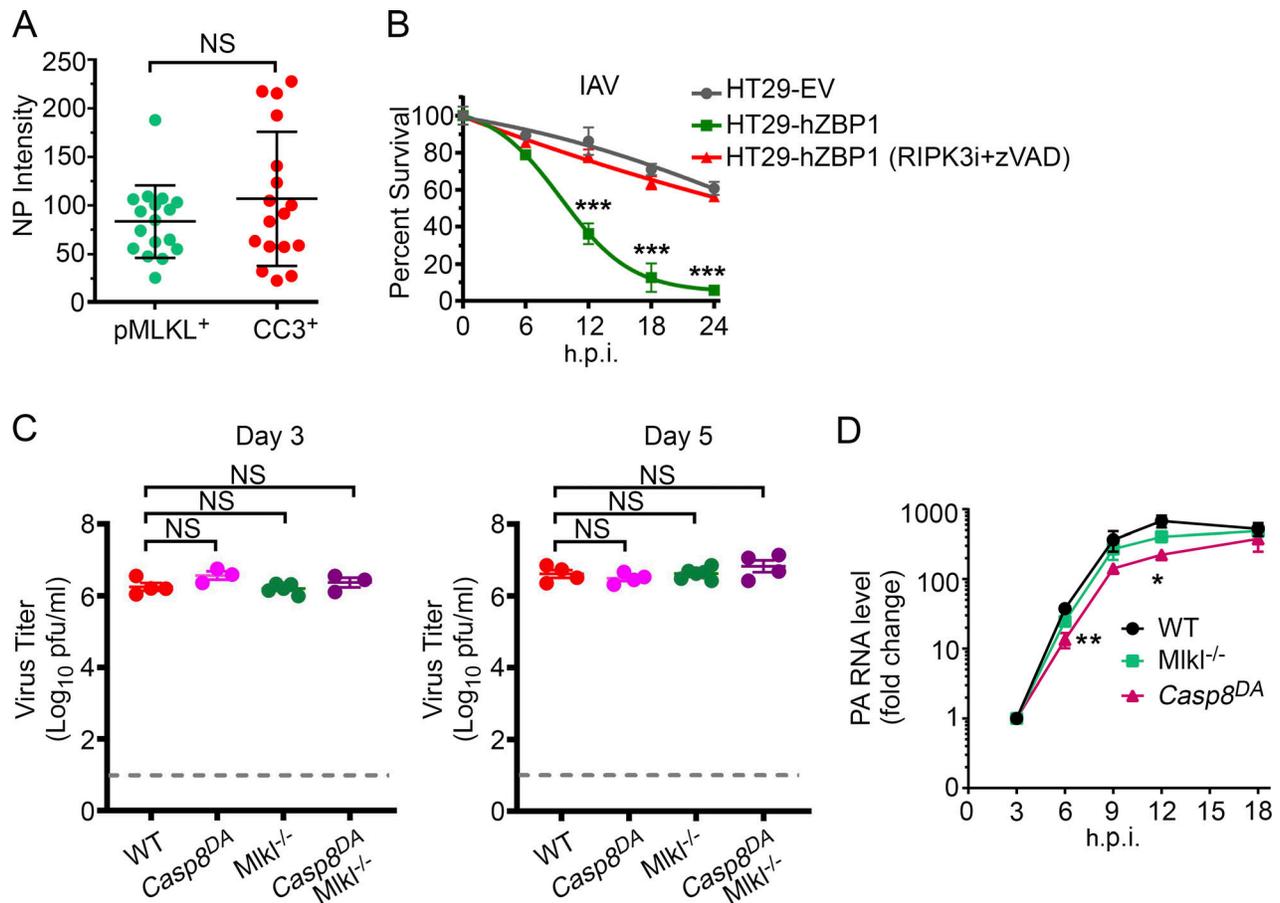
Figure S2. **Characterization of virus replication in cells and in vivo. (A)** Quantification of NP signal intensity in IAV-infected WT MEFs (PR8; MOI, 2; 18 h.p.i.) that are either pMLKL[+] or CC3^{+}. Of note, a few apoptotic (i.e., CC3^{+}) cells showed a markedly intense NP signal, likely because they had shrunk in size (characteristic of apoptosis) and therefore harbor a more condensed pool of NP. Data are pooled from three fields with 6–10 cells/field; data are from one of four experiments with similar results. **(B)** HT-29 FLAG-ZBP1 cells were produced by retroviral transduction of an expression vector encoding FLAG-tagged human ZBP1 into the HT-29 cell line. These cells, but not control cells expressing an empty vector (EV), underwent rapid cell death upon infection with PR8 (MOI, 2). IAV-induced cell death was dependent on ZBP1-RIPK3 signaling, shown by rescue with the combination of RIPK3i (GSK'843; 5 µM) + zVAD (50 µM). $n = 3$ replicates per condition; data are from one of six experiments with similar results. **(C)** Lung virus titers of mice of the indicated genotypes at 3 d.p.i. (left) or at 5 d.p.i (right) with PR8 (1,500 EID$_{50}$). WT, $n = 4$; $Casp8^{DA}$, $n = 3$; $Mlkl^{-/-}$, $n = 5$; $Casp8^{DA}Mlkl^{-/-}$, $n = 3$ for D3. WT, $n = 4$; $Casp8^{DA}$, $n = 4$; $Mlkl^{-/-}$, $n = 5$; $Casp8^{DA}Mlkl^{-/-}$, $n = 4$ for D5. **(D)** Kinetics of IAV (PR8; MOI, 2) replication in MEFs of the indicated genotypes as determined by quantitative RT-PCR analysis of PA segment levels. $n = 3$ replicates per condition; data are from one of six experiments with similar results. Unpaired Student's t test (A and D); two-way ANOVA with Tukey's multiple comparisons test (B); Mann-Whitney test (C). Error bars represent mean ± SD. *, $P < 0.05$; **, $P < 0.005$; ***, $P < 0.0005$.
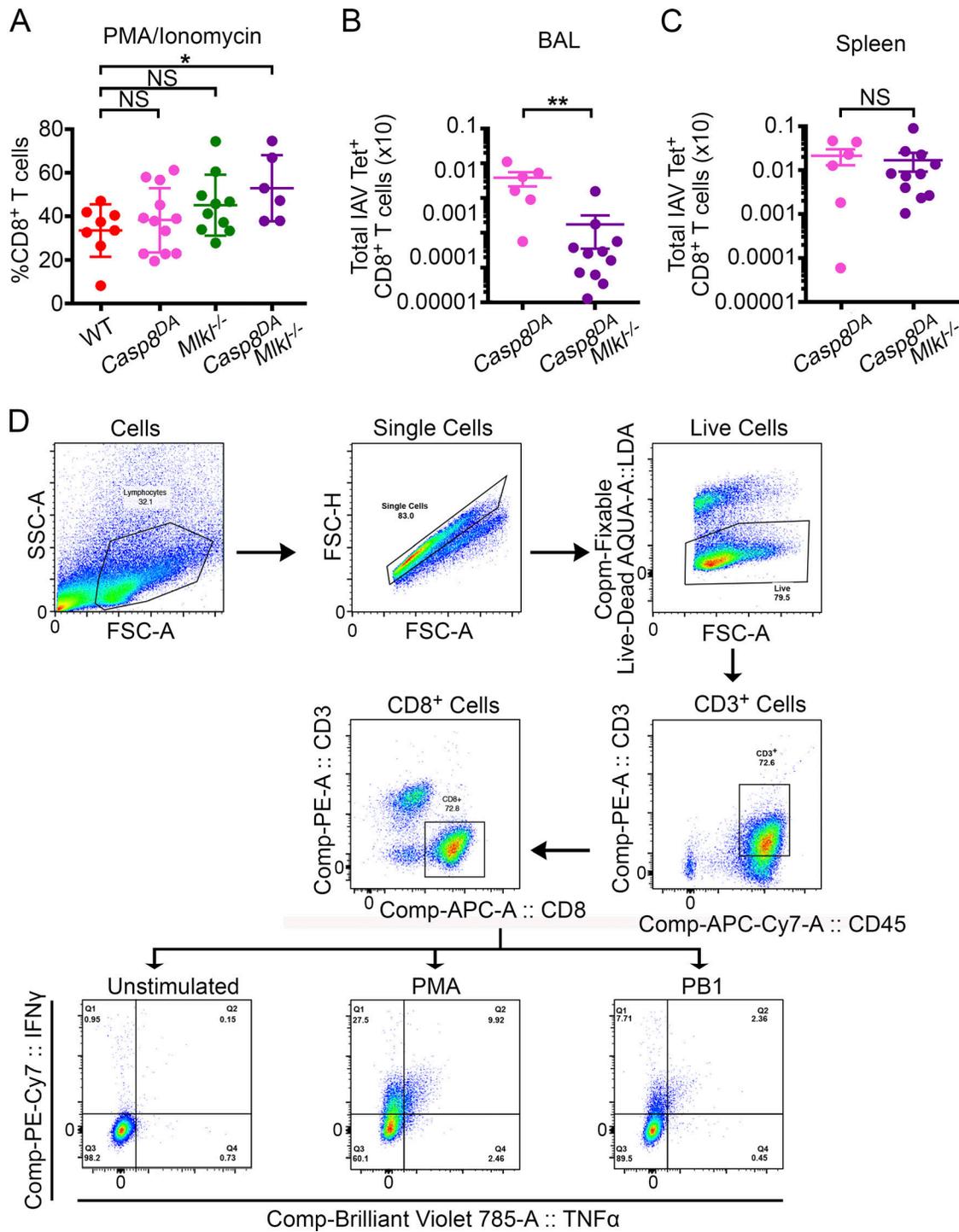
Figure S3. **CD8⁺ T cell activation defects in *Casp8^DA^Mlkl^−/−* mice are lung specific. (A)** Proliferation of CD8⁺ T cells from *Casp8^DA^Mlkl^−/−* mice is not impeded in response to the nonspecific stimulus PMA/ionomycin ex vivo. WT, $n = 8$; *Casp8^DA^*, $n = 12$; *Mlkl^−/−^*, $n = 10$; *Casp8^DA^Mlkl^−/−^*, $n = 6$. **(B)** Total IAV PB1$_{703-711}$ tetramer⁺ CD8⁺ T cells from the BAL of mice of the indicated genotypes collected at 8 d.p.i. with PR8 (1,500 EID$_{50}$). *Casp8^DA^*, $n = 6$; *Casp8^DA^Mlkl^−/−^*, $n = 11$. **(C)** Total IAV PB1$_{703-711}$ tetramer⁺ CD8⁺ T cells from the BAL of mice of the indicated genotypes collected at 8 d.p.i. with PR8 (1,500 EID$_{50}$). *Casp8^DA^*, $n = 6$; *Casp8^DA^Mlkl^−/−^*, $n = 11$. **(D)** Gating strategy used in this figure and in Fig. 4. Data are representative of two independent experiments (A–C). One-way ANOVA comparing WT samples with every other genotype (A–C). *, $P < 0.05$; **, $P < 0.005$. FSC, forward scatter; SSC, side scatter.